

Resonant X-ray Scattering Study of Magnetic and Electric-quadrupole Order in $U_{0.75}Np_{0.25}O_2$

S. B. Wilkins,^{1,2} J. A. Paixão,³ R. Caciuffo,^{1,4} P. Javorsky,¹ F. Wastin,¹
J. Rebizant,¹ C. Detlefs,² N. Bernhoeft,⁵ P.Santini,⁶ and G. H. Lander¹

¹*European Commission, Joint Research Centre,
Institute for Transuranium Elements,
Postfach 2340, Karlsruhe, D-76125 Germany*

²*European Synchrotron Radiation Facility,
Boîte Postal 220, F-38043 Grenoble CEDEX, France*

³*Physics Department, University of Coimbra, Coimbra, 3004-516 Portugal*

⁴*Dipartimento di Fisica ed Ingegneria dei Materiali e del Territorio,
Università Politecnica delle Marche, I-60131 Ancona, Italy*

⁵*Département de la Recherche Fondamentale sur la Matière Condensée,
CEA, F-38054 Grenoble CEDEX, France*

⁶*Dipartimento di Fisica, Università di Parma,
Viale Parco delle Scienze, I-43100, Parma, Italy*

(Dated: June 24, 2018)

Abstract

We have used element specific X-ray resonant scattering to investigate the M edge resonances in a single crystal of $\text{U}_{0.75}\text{Np}_{0.25}\text{O}_2$. Earlier neutron diffraction and Mössbauer studies had shown the presence of long-range AF order below $T_N = 19$ K, with sizeable magnetic moment both on the U and the Np ions. RXS results confirm the presence of an ordered dipole magnetic moment on the Np ions, but also reveal the presence of an anti-ferro arrangement of the electric quadrupole moments on both U and Np ions, with the same propagation vector that defines the magnetic structure. From the azimuthal dependence of the intensities we are able to determine the exact configuration of the quadrupolar ordering. The intensities of Bragg peaks associated with magnetic dipole and electric quadrupole order have different temperature dependences. On cooling below T_N , the magnetic dipole order develops faster on the uranium ions, with magnetic order on the Np ions increasing at a lower rate. At the same temperature, quadrupolar order on both the U and Np ions occurs along with an internal Jahn-Teller lattice distortion.

PACS numbers: 75.25.+z, 75.10.-b

I. INTRODUCTION

Actinide dioxides, AnO_2 , have fascinating physical properties whose understanding is still a challenge, despite half a century of extensive investigations carried out by both theoreticians and experimentalists. The complexity of their physical behavior stems from the subtle interplay between crystal field (CF), superexchange interactions and electron-phonon coupling, which results in peculiar multi-polar ordered-phase diagrams.

At room temperature AnO_2 systems have the *fcc* crystal structure of CaF_2 , with space group $Fm\bar{3}m$ and tetravalent An^{4+} ions. Ordered magnetism below $T_N = 30.8 K$ was suggested in UO_2 by the presence of a large anomaly in the temperature dependence of the heat capacity¹, and confirmed by magnetic susceptibility² and neutron diffraction^{3,4} measurements. Neutron spectroscopy was soon after applied to elucidate collective excitations, vibrational and magnetic, in the low temperature phase⁵. Evidence of a strong spin-lattice interaction prompted a theory introducing the concepts of Jahn-Teller (J-T) effects and electric quadrupole interactions in the actinide materials⁶. Some years later, neutron diffraction actually revealed an internal J-T distortion of the oxygen sub-lattice in UO_2 ⁷, and eventually it was demonstrated that the magnetic structure is $3\text{-}\mathbf{k}$ type, i.e. Fourier components of all three members of the star of $\mathbf{k} = \langle 001 \rangle$ are *simultaneously* present on each magnetic site of the lattice.⁸ These Fourier components of the magnetic moment, $\boldsymbol{\mu}_k$, are perpendicular to the propagation vector \mathbf{k} , so that the structure is *transverse*. The overall symmetry remains cubic, and the magnetic moments $\boldsymbol{\mu}_0$ point along the [111] directions of the cubic unit cell. As $\boldsymbol{\mu}_k$ can assume two mutually orthogonal directions for each \mathbf{k} value (for instance, $\boldsymbol{\mu}_k$ parallel to [010] or [001] for $\mathbf{k} = [100]$), there two distinct $3\text{-}\mathbf{k}$ transverse magnetic structures (Figure 1).

Experiments on powder samples with chopper spectrometers at spallation neutron sources allowed a precise and reliable determination of the CF Hamiltonian acting on the U ions⁹, and experiments with triple-axis spectrometers and axial polarization analysis have been performed to study collective excitations in the ordered phase, and dispersive magnetic excitons in the paramagnetic phase¹⁰. The experimental picture is therefore exhaustive, but a satisfying theoretical description of low-temperature collective excitations is still missing.

Magnetic order was expected to occur also in NpO_2 , for which a large λ -like anomaly in the heat capacity¹¹ and a maximum in the magnetic susceptibility curve¹² were observed at $T_0 =$

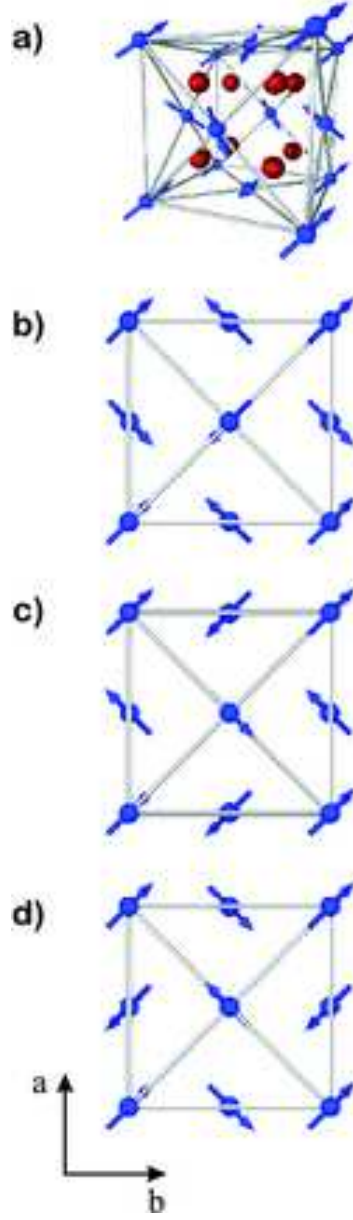


FIG. 1: a) Shows a 3d representation of the $3\text{-}\mathbf{k}$ magnetic structure. Uranium atoms are shown as blue spheres with the corresponding dipole magnetic moment direction shown as an arrow. Oxygen atoms are shown as red spheres. b) The longitudinal $3\text{-}\mathbf{k}$ structure as projected onto the $a - b$ plane, i.e. on moving from an atom at (000) with a moment along $[111]$ to the atom at $(\frac{1}{2}\frac{1}{2}0)$ the moment direction changes to $[\bar{1}\bar{1}\bar{1}]$. c) and d) are transverse structures. Following the reasoning above the atom situated at $(\frac{1}{2}\frac{1}{2}0)$ has moment directions $[\bar{1}1\bar{1}]$ and $[1\bar{1}\bar{1}]$ for c) and d) respectively.

25 K. However, neither Mössbauer spectroscopy¹³ nor neutron diffraction experiments^{14,15,16} have found evidence of magnetic ordering in this compound. The experiments set an upper

limit on the Np ordered magnetic moment of $0.01 \mu_B$, a value that is surprisingly small given the Kramers nature of Np^{4+} ions ($5f^3, {}^4I_{9/2}$ in Russell-Saunders approximation), and the large effective Curie-Weiss paramagnetic moment deduced from susceptibility measurements ($\sim 3 \mu_B$).

Indeed, Resonant X-ray Scattering (RXS) experiments¹⁷ at the Np M_4 edge exclude usual magnetic dipole ordering at T_0 , but provide direct evidence of long-range order of an electric quadrupole moment with Γ_5 symmetry. The phase transition is purely electronic and involves neither internal nor external crystallographic distortions, so the symmetry of the system remains cubic^{16,18,19}. It has been suggested that the primary order parameter is associated with Γ_4^t magnetic octupoles, ordering in a $3\text{-}\mathbf{k}$ *longitudinal* structure with $\langle 001 \rangle$ propagation vector. The ground state (GS) is a singlet with no static dipole magnetic moment in which magnetic octupole order breaks time reversal invariance and induces an electric quadrupole as the secondary order parameter^{20,21}.

The magnetic behavior of $\text{U}_{1-x}\text{Np}_x\text{O}_2$ solid solutions has also been extensively investigated by powder neutron diffraction, ^{237}Np Mössbauer spectroscopy, and magnetic susceptibility measurements^{22,23,24}. The ^{237}Np Mössbauer isomer shift indicates that Np ions are tetravalent, with $5f^3, {}^4I_{9/2}$ electronic configuration, independently of temperature and composition. Magnetic order has been detected in the composition range from $x = 0.15$ and $x = 0.75$, with transition temperatures decreasing with increasing x , from $T_N \approx 17$ K ($x = 0.25$) to $T_N \approx 11$ K ($x = 0.75$), showing that substitution of Np for U reduces the strength of U-U exchange interactions. For $x = 0.25$, the magnetic structure is transverse antiferromagnetic type I, as in UO_2 , with propagation vector $\langle 001 \rangle$, and an average ordered magnetic moment $\mu = 1.8(1)\mu_B$. As Mössbauer data are compatible with an ordered magnetic moment $\mu_{\text{Np}} = 0.6(2)\mu_B$ on the Np ions, this gives $\mu_{\text{U}} = 2.2(2)\mu_B$ on the U ions. For larger Np content, the magnetic order is short range and incommensurate²².

II. RESONANT X-RAY SCATTERING

Resonant X-ray Scattering (RXS) occurs when a photon is virtually absorbed by exciting a core electron to empty states, and subsequently re-emitted when the excited electron and the core hole recombine^{25,26}. This process introduces anisotropic contributions to the X-ray susceptibility tensor²⁷, the amplitude of which increases dramatically as the photon energy

is tuned to an atomic absorption edge. In the presence of long-range order of magnetic moments, electronic orbitals occupancy, or spatially anisotropic valence-electron clouds, the interference of the anomalous anisotropic scattering amplitudes may lead to the excitation of Bragg peaks at positions forbidden by the crystallographic space group. For absorbing atoms belonging to the actinide series, both L- and M-edges are of practical use, as their energy is large enough for Bragg diffraction to be allowed in most actinide compounds. The experiments reported here have been performed at the U and Np M_4 and M_5 edges, involving respectively $3d_{3/2} \leftrightarrow 5f$ and $3d_{5/2} \leftrightarrow 5f$ electric-dipole, E1, virtual excitations.

The amplitude of *magnetic* scattering from a given atom at the $3d - 5f$ threshold is the product of a geometrical factor, depending on the polarization of the incident (ϵ) and scattered (ϵ') photons, and a linear combination of resonance strength factors, $F_{L,M}$,

$$F^{[1]} \propto (\epsilon \times \epsilon') [F_{1,1} - F_{1,-1}] \quad (1)$$

Magnetic scattering therefore requires a rotation of the photon polarization, and a difference in the transition probabilities to intermediate states with $M = \pm 1$. This asymmetry can arise because of the net spin polarization of the $5f$ states, or from a difference between overlap integrals, resonant energy, or lifetime for spin-up and spin-down channels^{26,28,29}.

RXS can also signal long-range order of anisotropic charge distributions. It is the asphericity of the atomic electron density that generates the anomalous tensor component in the atomic scattering factor. If the electron clouds on different sublattices have different orientations, superlattice reflections occur due to the reduced translational symmetry. This is the so-called Templeton or ATS (Anisotropic Tensor Susceptibility) scattering³⁰ and is observed, for instance, in case of antiferro-electric order of the quadrupole moments. The scattering amplitude arising from E1 transitions can be described by second-rank tensors $f(\mathbf{r})$, invariant under the point symmetry of the scattering atom. If $\tilde{f}(\mathbf{Q})$ is the Fourier transform of $f(\mathbf{r})$, the scattering amplitude can be written as

$$F^{[2]}(\mathbf{Q}) \propto \epsilon' \cdot \tilde{f}(\mathbf{Q}) \cdot \epsilon, \quad (2)$$

where ϵ and ϵ' are the polarization vectors of the incident and scattered beam, where the rotation about the azimuth is implicitly included in the electric field vector.

III. EXPERIMENTAL DETAILS

$\text{U}_{0.75}\text{Np}_{0.25}\text{O}_2$ single crystals have been grown using the chemical-transport reaction method at the Institute for Transuranium Elements in Karlsruhe. Starting materials were obtained by stoichiometric co-precipitation by ammoniac, calcination under air at 1073 K, followed by reduction under Ar/H₂ (5%) at 1073 K. Pellets were fabricated and sintered at 1973 K for 6 hours in Ar/H₂ atmosphere. Charges of about 5 g of starting material were crushed and welded in a quartz tube with TeCl₄ (4.5 mg/cm³) as transport agent in a 10⁻⁶ torr vacuum. The feed substances were maintained at 1323 K and transported under the influence of the temperature gradient into the growth region at 1223 K for 14 days. The single crystals obtained were characterized by chemical analysis, scanning electron microscopy, single crystal x-ray diffraction and x-ray diffraction on a powder obtained from crushed crystals. No differences in the average composition or evidence for clustering effects have been observed by these techniques. However, differences in the spatial homogeneity of the Np ions distribution in individual crystals grown by the method described above cannot be excluded.

Two specimens with a mass of 5.20 mg and 3.63 mg have been selected to measure the heat capacity as a function of temperature and magnetic field amplitude, using a PPMS-9 Quantum Design platform. The RXS experiment has been performed on the ID20 beamline of the European Synchrotron Radiation Facility (ESRF) in Grenoble, France. For these measurements we used a crystal 0.204 mm³ in volume, with a mass of 2.26 mg and the [111] axis perpendicular to the exposed face. The sample was of excellent quality with a mosaic width of 0.05 °. For safety requirements, the crystal was encapsulated in a sealed double-wall container with beryllium windows.

The ID20 spectrometer exploits the fundamental harmonic emission of two 42-mm-period undulators. A double crystal Si(111) curved monochromator provides sagittal focusing and selects the appropriate X-ray energy. Vertical focusing and filtering of higher harmonics is achieved by Si mirrors, that deliver at the sample position a 99 % linearly polarized beam, with polarisation perpendicular to the scattering plane (σ) and incident wavevector \mathbf{k}_i . A mosaic crystal positioned between sample and detector was used to analyze whether the polarization of the scattered beam (with wavevector \mathbf{k}_f) is parallel (π) or perpendicular (σ) to the vertical scattering plane.

A closed-cycle refrigerator equipped with an azimuthal-rotation stage provided a base temperature of 10 K and the possibility to perform azimuthal scans. The spectrometer was operated in the photon energy interval from 3.5 to 4.0 keV, including the U and Np M -edges (U: $E_{M_5} = 3.552$ keV, $E_{M_4} = 3.728$ keV; Np: $E_{M_5} = 3.664$ keV, $E_{M_4} = 3.845$ keV), using the (111) reflection from a Au analyzer (Bragg angle of 43.2° at the Np M_4 edge, and 41.6° at the U M_4 edge; no correction was performed to account for the departure from the ideal 45° orientation of the analyzer crystal). The energy resolution was about 0.5 eV (full width at half maximum), and the beam flux at 3.845 keV was estimated as 5×10^{11} photons s^{-1} . Integrated intensities I_m for Bragg reflections were obtained numerically, by fitting a linear background and a Lorentzian squared lineshape to the measured peaks. Corrections for the size of the footprint of the incident beam and for absorption were applied as $I_c = I_m \mu(1 + \sin \alpha / \sin \beta)$, where α and β are the angles formed by the incident and scattered beam directions with the sample surface, and μ is the energy dependent absorption coefficient. Because of the strong absorption all reflections must be found in Bragg geometry.

IV. RESULTS OF THE EXPERIMENT

Figure 2 shows the heat capacity as a function of temperature measured for the $U_{0.75}Np_{0.25}O_2$ sample with 5.20 mg mass. Data were collected from 0.7 to 300 K in zero field and under an external magnetic field of 9 T. The base temperature was limited by self-heating effects, that become sizeable below 3 K. Contributions to the measured heat capacity from the sample platform (including grease used to establish thermal contacts) were measured separately and subtracted from the total signal. The results reveal the presence of a λ -like cusp at 18.9 K, and two small anomalies at 16.8 K, and 15 K. The application of a 9 T magnetic field does not produce appreciable effects; the maximum at 18 K undergoes a very small shift to a lower temperature while its amplitude slightly decreases. The specific heat of the isostructural compound ThO_2 is assumed to be a close estimate of the vibrational contribution, and is shown as a solid line in Figure 2. As previously reported for both UO_2 and NpO_2 ¹¹, the magnetic contribution is appreciably different from zero at temperatures far above the anomaly also in the solid solution.

The broken line in Figure 2 represents the results of measurements performed on a second single-crystal with the same nominal composition of the first one. The curves obtained for

the two samples are quite different; for the second one, the main anomaly occurs at 16.8 K, whereas small anomalies are visible at 18.4 K and 15 K. The characterization analysis suggests the same stoichiometry within experimental errors, and X-ray diffraction does not show line broadening, thus excluding major clustering effects. On the other hand, the subtle interplay between magnetic and electric multipolar interactions in this system could be very sensitive to even small changes in the chemical short-range order. The large difference observed in the heat capacity of the two samples could therefore reflect small variations in the probability distribution of Np neighbors around U ions.

The presence in the diffraction pattern of resonant superlattice reflections with propagation vector $\langle 001 \rangle$, forbidden in the paramagnetic phase, proves that long-range order of some multipolar moment characterizes the low-temperature ground state. The integrated intensity of the (112) Bragg peak at 10 K is shown as an example in Figure 3, as a function of the photon energy across the U and the Np M_5 and M_4 absorption edges. These data were collected without analyzing the polarization of the diffracted beam, and therefore represent the sum of the intensities in the $\sigma \rightarrow \sigma$ and $\sigma \rightarrow \pi$ polarization channels. The spectrum can be reproduced as the superposition of four oscillators that interfere with each other. The solid line in Figure 3 is obtained by assigning to each oscillator a Lorentzian lineshape centered at the E1 electric-dipole energy, including corrections for self-absorption and energy dependence of the beam attenuation.

At 10 K, a resonant behavior has been observed for both the $\sigma \rightarrow \pi$ and the $\sigma \rightarrow \sigma$ components of the spectrum. This is shown in Figures 4 and 5, around the U and the Np M_4 edge, respectively. Note that the $\sigma \rightarrow \sigma$ have Lorentzian squared lineshapes, and are shifted by -2 eV wrt. the $\sigma \rightarrow \pi$ peak. This has been previously observed in systems where the $\sigma \rightarrow \sigma$ signal is known to originate from the $F^{[2]}$ term.³¹ The ratio between the intensities of the $\sigma \rightarrow \sigma$ and the $\sigma \rightarrow \pi$ peak is about 30% for Np, and about 3% for U. For strictly magnetic *dipole* ordering, there is no signal in the $\sigma \rightarrow \sigma$ channel. Thus, the finite ratio indicates that the structurally forbidden peaks do *not* stem *uniquely* from dipole magnetic-order. Our RXS results are compatible with dipole magnetic-order together with an ordered distribution of electric quadrupole moments. Resonant scattering from orientationally ordered aspherical electron clouds appears in both polarization channels. On the other hand, the shape of the resonance across the M_4 absorption edge is different for the $\sigma \rightarrow \sigma$ and the $\sigma \rightarrow \pi$ contributions. Whilst the $\sigma \rightarrow \pi$ peak can be fitted to a Lorentzian

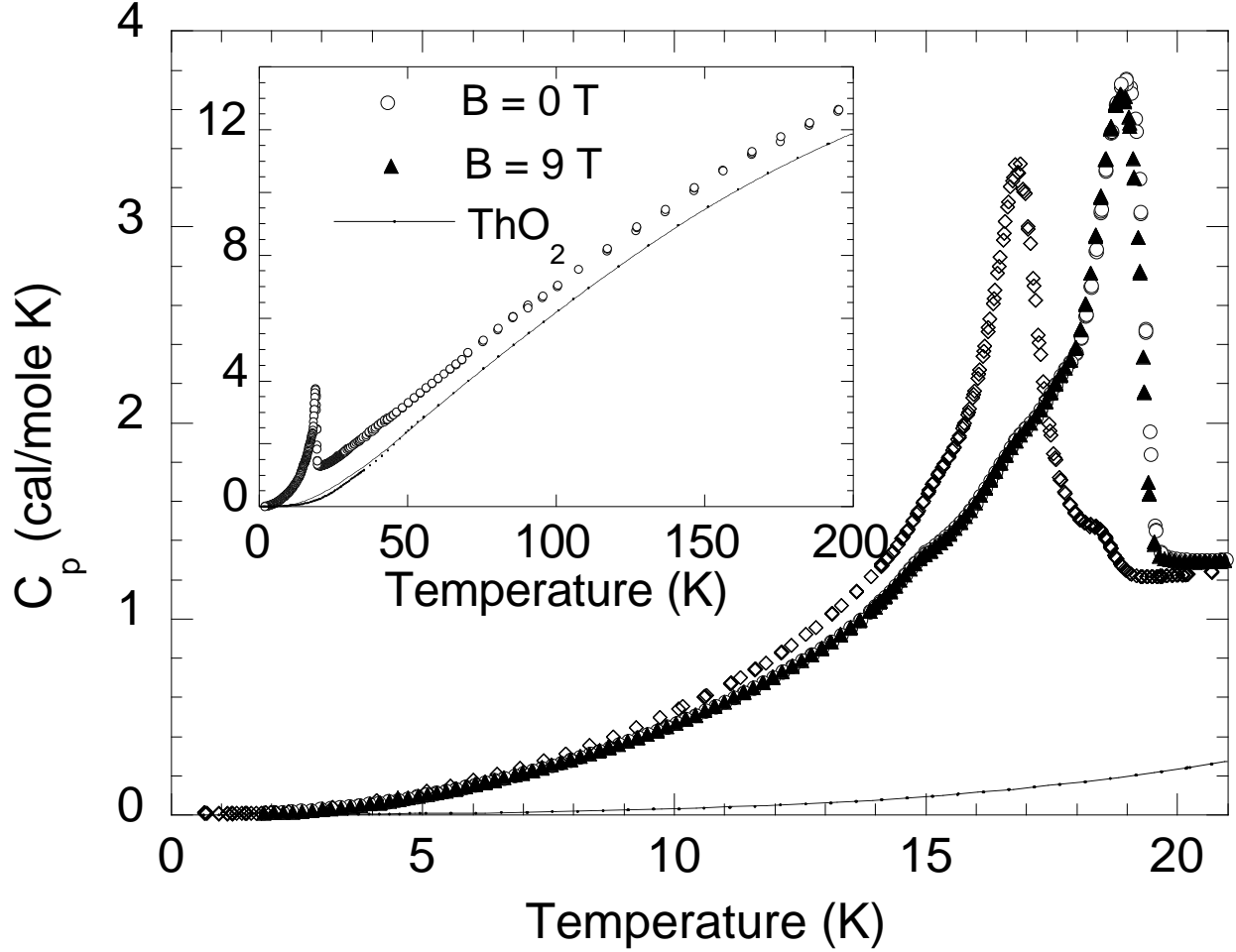


FIG. 2: Heat capacity measurements performed with a Quantum Design PPMS-9 system. Data were taken in an applied field of (circles) 0 T and (triangles) 9 T. A λ -like peak and two anomalies are clearly visible. The solid line is a fit to heat capacity data measured for the non-magnetic isostructural compound ThO_2 . The broken line corresponds to results obtained for a second sample with the same nominal composition.

function, the $\sigma \rightarrow \sigma$ resonance has a Lorentzian-squared lineshape. A Lorentzian peak is usually observed when the intensity enhancement is due to dipole magnetic order, whereas a Lorentzian-squared peak has been observed in NpO_2 , both in the rotated and the unrotated polarization channel¹⁷.

The narrow energy profile of the Bragg intensity at the Np M_4 edge in NpO_2 has been associated with a $3d_{3/2}$ core-level structure, and attributed to magnetic and charge contributions to the E1 Bragg amplitude described by Np 5f multipoles of rank 3 and 4³⁸. This explanation cannot be applied in the present case, as U^{4+} ions in UO_2 do not carry

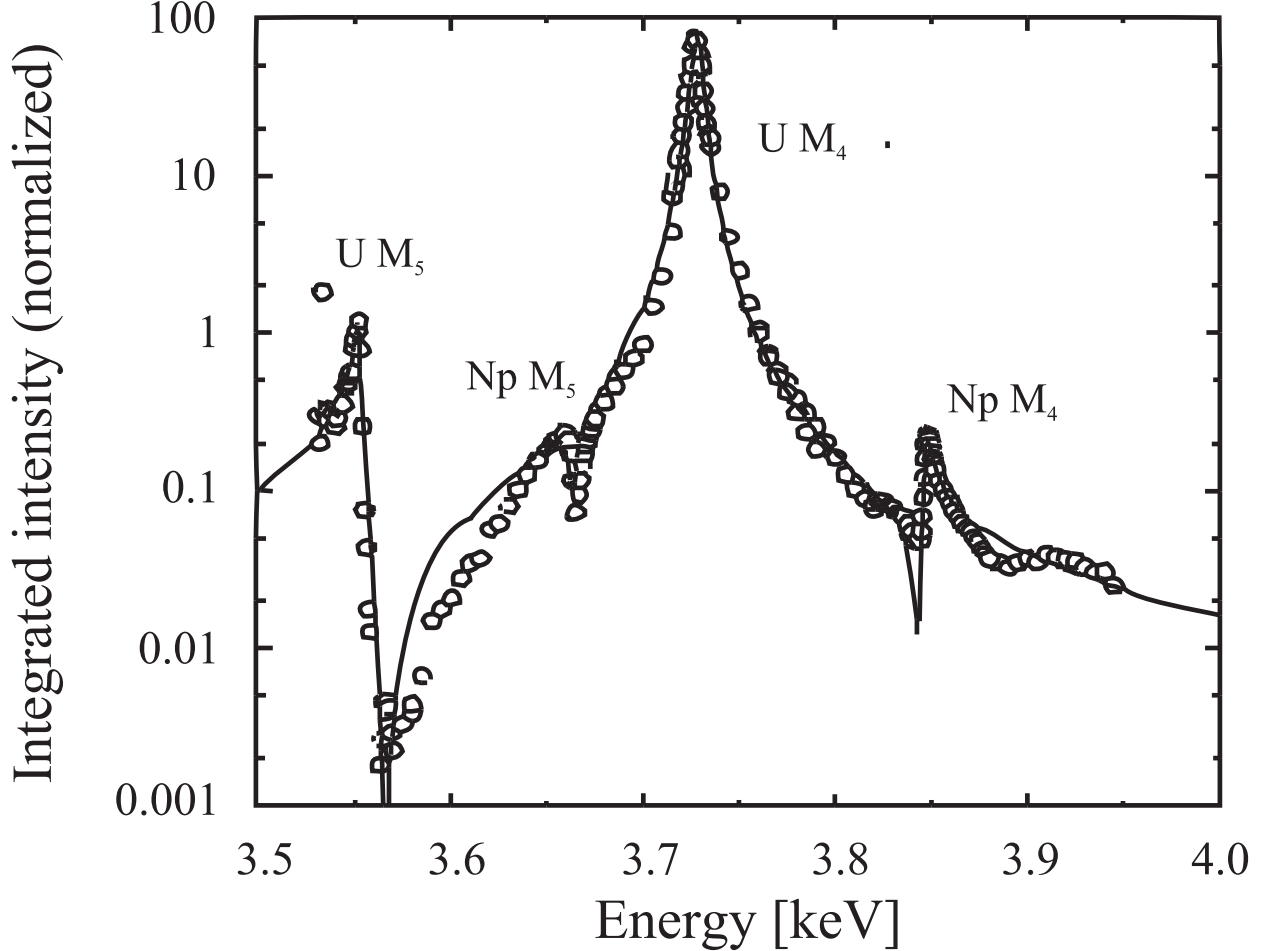


FIG. 3: Normalized integrated intensity as a function of energy for the (112) reflection of $\text{U}_{0.75}\text{Np}_{0.25}\text{O}_2$ at 10 K. Polarization analysis was not performed. The solid line is a simulation assuming four dipole oscillators, each represented by a Lorentzian function.

magnetic octupoles. On the other hand, in ref. 17 the RXS signal observed in NpO_2 is interpreted entirely as a consequence of electric-quadrupole order, both for the $\sigma \rightarrow \sigma$ and the $\sigma \rightarrow \pi$ channels, as the magnetic ordered moment in NpO_2 is vanishingly small. The results presented here seems to support these latter interpretations.

As the magnetic ordered moment in NpO_2 is vanishingly small, in that case the resonant scattering is entirely due to electric-quadrupole order. It therefore appears that the Lorentzian squared shape is a characteristics of quadrupole order in these compounds. We conclude that in this solid solution, the $\sigma \rightarrow \pi$ signal is dominated by the magnetic dipole contribution, whilst the $\sigma \rightarrow \sigma$ resonance is due only to the electric-quadrupole order.

The results of Ψ (azimuthal) scans about the (112) magnetic peak, taken at $T = 10$ K with

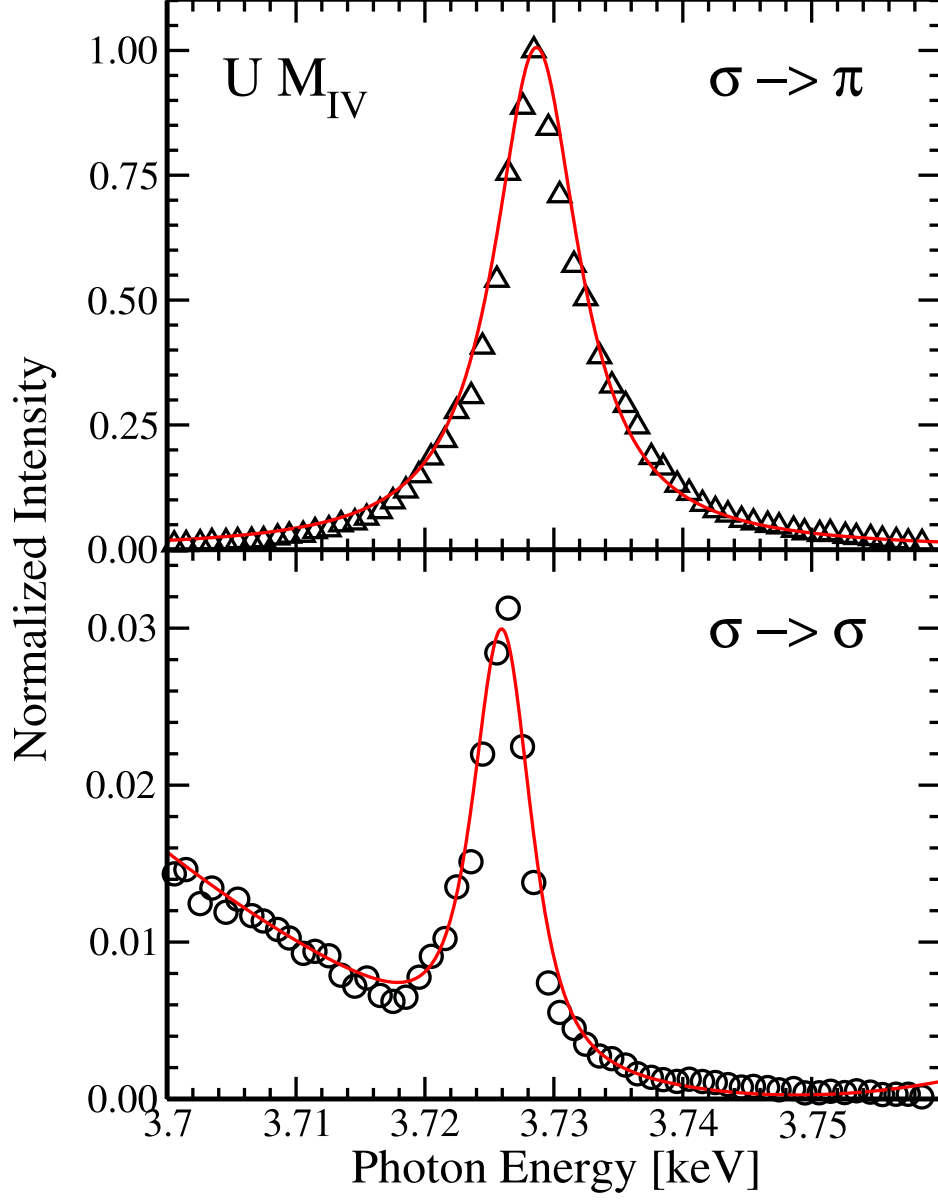


FIG. 4: Integrated intensity of the (112) superlattice reflection, at 10 K, as a function of photon energy in the vicinity of the $U M_4$ absorption edge. Upper panel $\sigma \rightarrow \pi$ lower panel $\sigma \rightarrow \sigma$. The solid line (upper panel) is a fit to a Lorentzian lineshape with a FWHM of 8 eV. In the lower panel the solid line represents a fit to a Lorentzian squared lineshape with the same width and a sloping background.

photons energy tuned to the Np and $U M_4$ edges, are shown in Figure 6. The intensity of the peak is measured while the sample is rotated about the scattering vector \mathbf{Q} , kept constant at the chosen value. The origin of the azimuthal angle, Ψ , is defined where the $[11\bar{1}]$ -direction

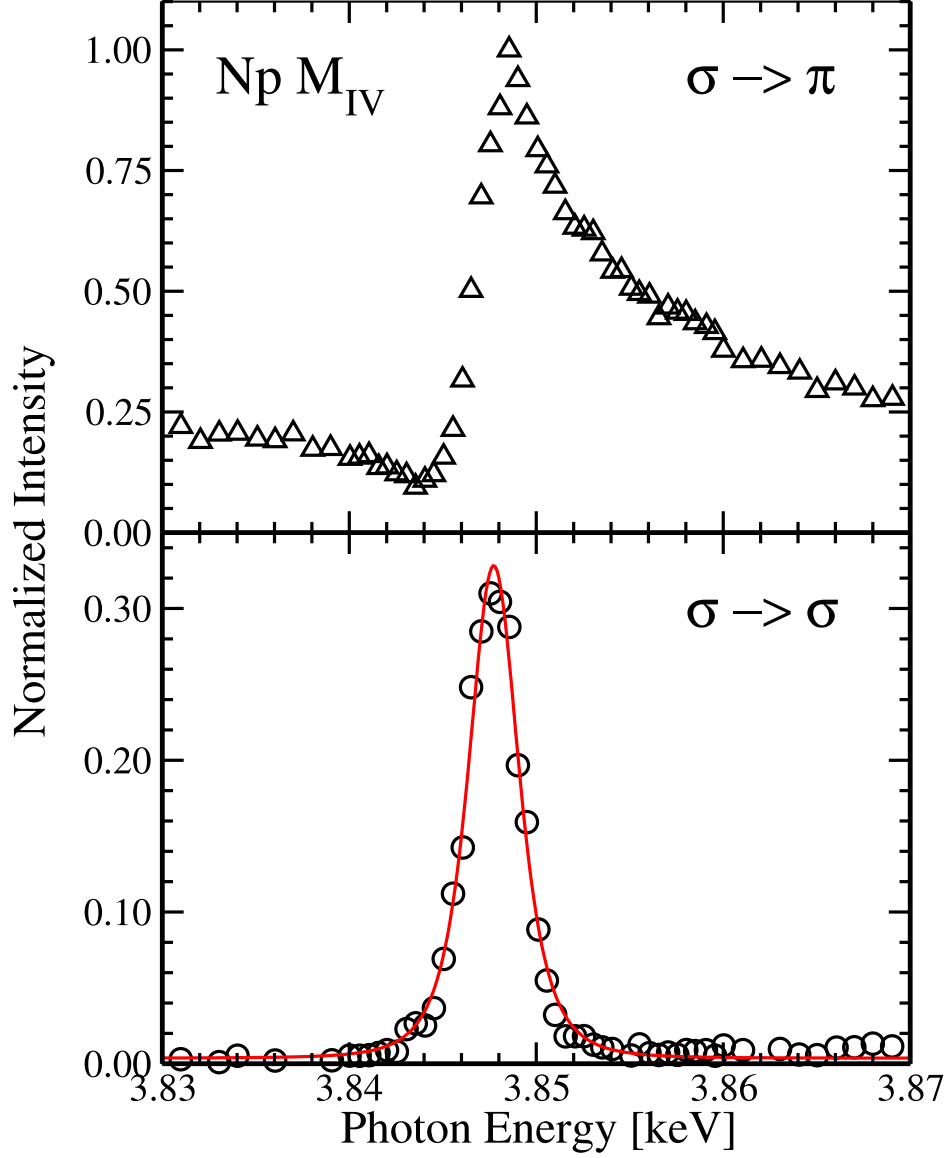


FIG. 5: Integrated intensity of the (112) superlattice reflection, at 10 K, as a function of photon energy in the vicinity of the Np M_4 absorption edge. Upper panel $\sigma \rightarrow \pi$ lower panel $\sigma \rightarrow \sigma$. The solid line (lower panel) show a fit to a Lorentzian squared lineshape. The $\sigma \rightarrow \pi$ contribution is dominated by the magnetic dipole signal and exhibits a Lorentzian lineshape (upper panel). Intensities are normalized to the maximum of the $\sigma \rightarrow \pi$ signal at the M_4 dipole threshold. Note that the $\sigma \rightarrow \pi$ signal (upper panel) is strongly influenced by the dominant signal from the U M_4 resonance, see Figure

is within the scattering plane. Oscillations with two-fold symmetry are observed for both the U and Np signals in the $\sigma \rightarrow \sigma$ channel. On the other hand, the $\sigma \rightarrow \pi$ intensities are independent of Ψ . The azimuthal dependence of the peak intensity is similar at the U and Np M_4 edges, indicating the same electric quadrupole orientation on the two ions.

The solid line in Figure 6 is a simulation of the scattered intensity for a $3\text{-}\mathbf{k}$ anti-ferroquadrupole structure assuming an incoherent addition of the two transverse s-domains (See Figure 1). The lower panel of Figure 6 shows a simulation of the longitudinal $3\text{-}\mathbf{k}$ anti-ferroquadrupole structure. This model clearly does not fit the data. Details of the calculations used to obtain the simulated azimuthal dependence are given in the appendix.

Figure 7 shows the temperature dependence of the (112) integrated intensities, normalised to unity at 10 K. The reported data were taken at the M_4 dipole threshold of either Np or U, for both polarization channels. Intensity was collected as a function of time while the sample temperature was varied at a rate of 2 K min^{-1} . The $\sigma \rightarrow \pi$ intensity is dominated by the magnetic dipole contribution and is therefore proportional to the square of the ordered magnetic moment. The $\sigma \rightarrow \sigma$ channel intensity, on the other hand, is proportional to the square of the electric quadrupole order parameter.

On cooling, the magnetic-dipole order develops first on U at $T_N \approx 19 \text{ K}$; the order-parameter increases with an apparent plateau between T_N and 18 K. The magnetic order on Np, and electric quadrupole order of both ions, is established at T_N but the corresponding order-parameters increase at a lower rate. Note that the AF phase transition in UO_2 is strongly discontinuous, whereas in the solid solution the quadrupolar and the magnetic phase transition are continuous. The temperature dependence of the U $\sigma \rightarrow \pi$ and $\sigma \rightarrow \sigma$ intensity is remarkably different, whilst for Np the corresponding difference is marginal.

Besides resonant superlattice reflections, diffraction peaks corresponding to a deformation of the oxygen cube have also been found. The angular positions of the observed peaks corresponds to those expected for the inhomogeneous internal distortion observed in UO_2 ⁷, and resulting from combinations of normal modes of the oxygen sub-lattice. For these measurements, we used a photon energy of 7.5 keV and a Ge (333) analyser to select the $\sigma \rightarrow \sigma$ polarisation channel, where structural Bragg peaks give a contribution. As an example, we show in Figure 7 (solid line) the intensities measured for the internal lattice modulation measured at the (421) reflection. It appears that the onset of the Jahn-Teller distortion coincides with the onset of the $\sigma \rightarrow \sigma$ scattered intensity, i.e. the long range order

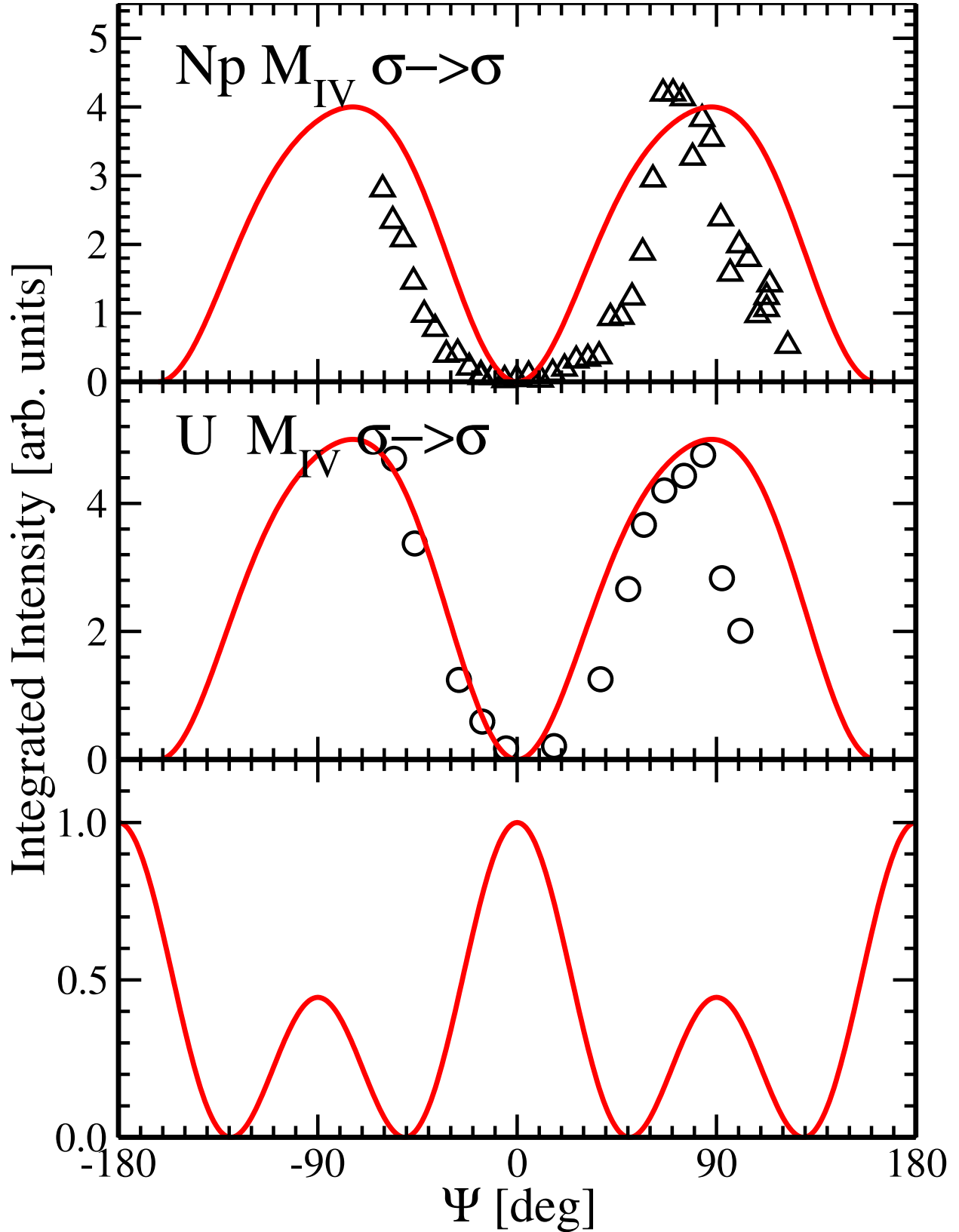


FIG. 6: Azimuthal dependence of the integrated intensity of the (112) superlattice reflection in the $\sigma \rightarrow \sigma$ channel at both the Np M_4 (top panel) and U M_4 (middle panel) absorption edges. Lines are intensities calculated assuming a electric quadrupole moments along the $\langle 111 \rangle$ direction, for a addition of two noncollinear transverse antiferro-quadrupolar domains (see Figure 1). The lower

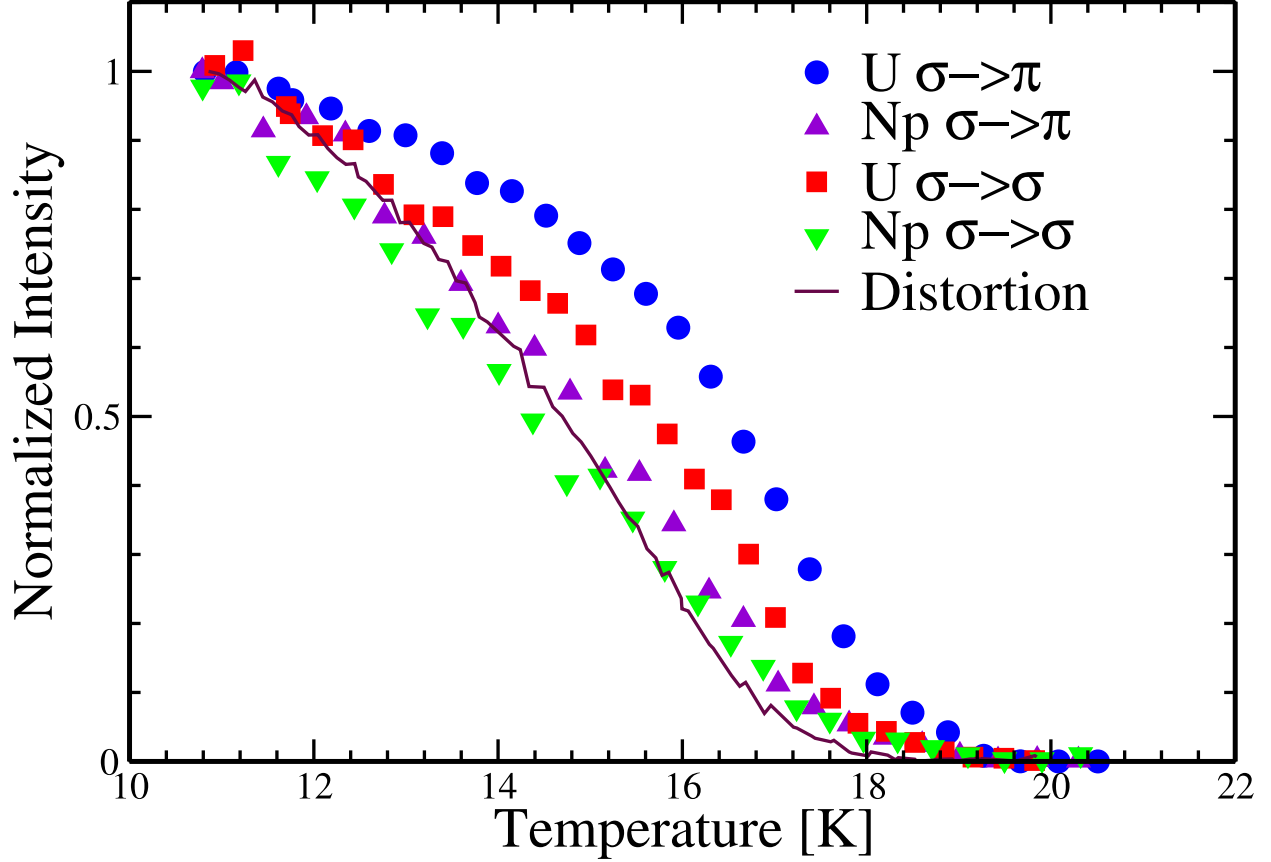


FIG. 7: Scattered intensity of the forbidden reflections as a function of temperature. The data for the (112) reflection were taken at the M_4 edges of U and Np in both polarization channels: (filled circles) U $\sigma \rightarrow \pi$ intensity; (open circles) U $\sigma \rightarrow \sigma$ intensity; (upper triangles) Np $\sigma \rightarrow \pi$ intensity; (down triangles) Np $\sigma \rightarrow \sigma$ intensity. The solid line intensities are measured for the (421) internal lattice modulation at 7.5 keV, indicating the onset of a Jahn-Teller distortion at T_N . Solid lines are fit to a power law.

of the electric quadrupolar moments.

A departure from the cubic symmetry was also checked by following angular position and width of the (006) lattice reflection, but no evidence for a lowering of symmetry was found. This confirms the $3\text{-}\mathbf{k}$ nature of the ordering. On the other hand, as shown in Figure 8, an anomalous volume contraction of the cubic cell is observed on cooling between T_N and 18 K.

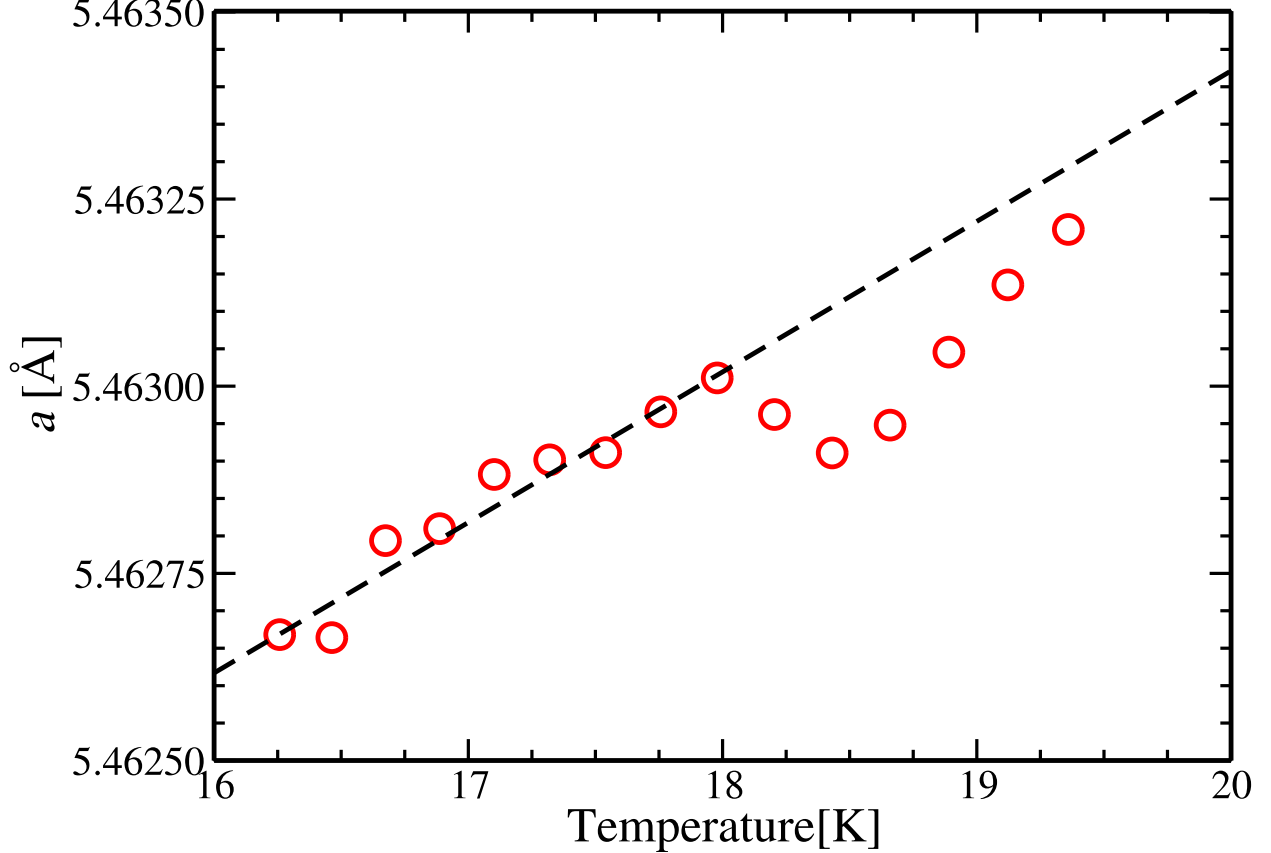


FIG. 8: Temperature dependence of the lattice parameter of the $U_{0.75}Np_{0.25}O_2$ solid solution. Error bars are smaller than the symbols. An anomalous contraction can be observed in the temperature interval between 18 and 20 K.

V. DISCUSSION

The CF spectrum of actinide dioxides is known with high degree of precision from inelastic neutron scattering (INS) experiments. The CF ground state of U in UO_2 is a Γ_5 triplet, whereas the CF ground state of Np in NpO_2 is a Γ_8 quartet. The CF potential changes little among UO_2 , NpO_2 , and even PuO_2 . Therefore, the CF acting upon the U and Np ions in solid solutions $U_xNp_{1-x}O_2$ is expected to be the same as in the pure compounds.

The Γ_5 triplet carries magnetic-dipole and electric-quadrupole degrees of freedom. U-U dipolar and quadrupolar interactions are provided by superexchange (SE) and additional U-U quadrupolar interactions are carried by phonons through the so-called virtual-phonon exchange. In UO_2 dipolar interactions are stronger than quadrupolar interactions and would produce on their own a second-order AF transition at around 25 K. A quadrupole moment

is induced by dipoles as secondary order parameter (OP). In turn, this quadrupole induces a lattice distortion of the oxygen cage. Although quadrupolar interactions are too weak to produce a purely quadrupolar phase transition, they contribute to the free energy of the system when quadrupoles are induced by dipoles. This contribution is believed to be responsible for the change of the magnetic transition from second- to first-order with an increase of T_N up to about 31 K. The AF structure, type-I transverse $3\text{-}\mathbf{k}$, is probably stabilized by quadrupolar interactions. As yet no theoretical model has been able to explain the occurrence of the $3\text{-}\mathbf{k}$ structure.

In NpO_2 , the Γ_8 quartet carries magnetic-dipole, electric-quadrupole and magnetic-octupole degrees of freedom. Np-Np dipolar, quadrupolar and octupolar interactions are provided by superexchange (SE) and additional Np-Np quadrupolar interactions are carried by phonons. The latter are expected to be appreciably smaller than the corresponding U-U interactions because of the smaller quadrupolar polarizability of Np ions. Dipole-dipole interactions are expected to be smaller as well³⁵. Octupolar interactions appear to dominate, and induce a second-order AF transition with no dipole moment, but with an associated quadrupole secondary OP. No lattice distortion occurs¹⁷.

Ion-ion interactions in solid solutions $\text{U}_x\text{Np}_{1-x}\text{O}_2$ are particularly rich. As a reasonable guess, U-U and Np-Np interactions may be assumed to be similar to those in pure compounds. The lack of a scaling framework for SE makes U-Np interactions difficult to estimate *a priori*. A few qualitative observations are formulated in the following from a virtual-crystal-approximation-like perspective, i.e. focusing on "average" properties and neglecting effects specifically associated with the disorder in the sample.

Since the magnetic phase transition of $\text{U}_{0.75}\text{Np}_{0.25}\text{O}_2$ occurs at a lower T_N than in UO_2 , Np acts as a magnetic diluent, and therefore U-Np dipolar interactions must be much smaller than the corresponding U-U interactions. Since adding Np makes the transition second-order, quadrupolar interactions must be smaller than in UO_2 . U-Np octupolar interactions are absent since octupoles are quenched in U. Thus, the phase transition of $\text{U}_{0.75}\text{Np}_{0.25}\text{O}_2$ is driven mainly by U-U dipolar interactions. U quadrupoles (and the associated lattice distortion) follow U dipoles as secondary OPs but their contribution to the free energy is too small to affect the phase transition qualitatively (i.e. to change the value of T_N and the order of the transition). Their slow rate of growth below T_N reflects a large β exponent, which is typical of a secondary OP linearly coupled to the square of the primary OP (in

mean-field β is twice the primary's OP β).

Np ions are expected to play a more passive role. The leading interaction of NpO₂, i.e. octupole-octupole, has no significant effects in U_{0.75}Np_{0.25}O₂ since it involves the minority Np-Np pairs but not U-Np and U-U pairs. As U ions order, Np ions feel the developing U dipoles and quadrupoles through U-Np interactions, and themselves acquire ordered dipoles and quadrupoles. The delay by which these Np moments are detected by X-rays can be understood quite naturally within this picture: since the U-Np dipolar interaction by which the U dipolar order is transmitted to Np ions is (relatively) weak, thermal fluctuations on Np ions are quenched by the phase transition more slowly than on U ions. So, Np moments appear at T_N together with U moments, but they grow more slowly as T decreases, although eventually as $T \rightarrow 0$ the full moments must be recovered.

In order to check this qualitatively, we performed calculations for the solid solution based on the virtual-crystal-approximation (VCA)³⁷. Russell-Saunders coupling was assumed, and for simplicity only the CF ground multiplets of U and Np were included in the calculation, neglecting therefore excited CF states. Although the wavefunctions of the Γ_8 quartet of Np depends on the cubic CF parameter x , results do not depend qualitatively on x ($x = -0.75$ was used²⁰). The VCA calculation assumed a $3\text{-}\mathbf{k}$ structure and contained four order parameters to be determined self-consistently at each temperature, i.e. the size of the dipole moment along $\langle 111 \rangle$ and of the axial quadrupole moment along $\langle 111 \rangle$ for U and Np, $M_{111}(U)$, $M_{111}(\text{Np})$, $Q_{111}(U)$, $Q_{111}(\text{Np})$. There are six parameters, i.e. the dipole-dipole (J) and quadrupole-quadrupole (K) interaction strengths for U-U pairs, for U-Np pairs and for Np-Np pairs. Np-Np couplings play a minor role since these pairs are in minority. The two leading dipole-dipole couplings $J(\text{U-U})$ and $J(\text{U-Np})$ are determined by the known transition temperatures of pure UO₂ and of the solid solution. If quadrupole-quadrupole interactions are assumed to be mainly lattice-transmitted, then $K(\text{U-Np})$ and $K(\text{Np-Np})$ can be obtained by scaling $K(\text{U-U})$ by using the known quadrupolar polarizability of Np ions. $K(\text{U-U})$ is the parameter most difficult to determine, because the role of quadrupole interaction in the $3\text{-}\mathbf{k}$ structure of pure UO₂ is not quantitatively clear.

As an example, we show in Figure 9 calculated RXS intensities for a parameter set with a fairly small value of $K(\text{U-U})$, i.e. about half the value which had been tentatively used in UO₂³⁶. β exponents are mean-field like in the VCA, $\beta = 0.5$ for U and Np dipoles and $\beta = 1$ for U and Np quadrupoles. The curves are in qualitative agreement with experiment,

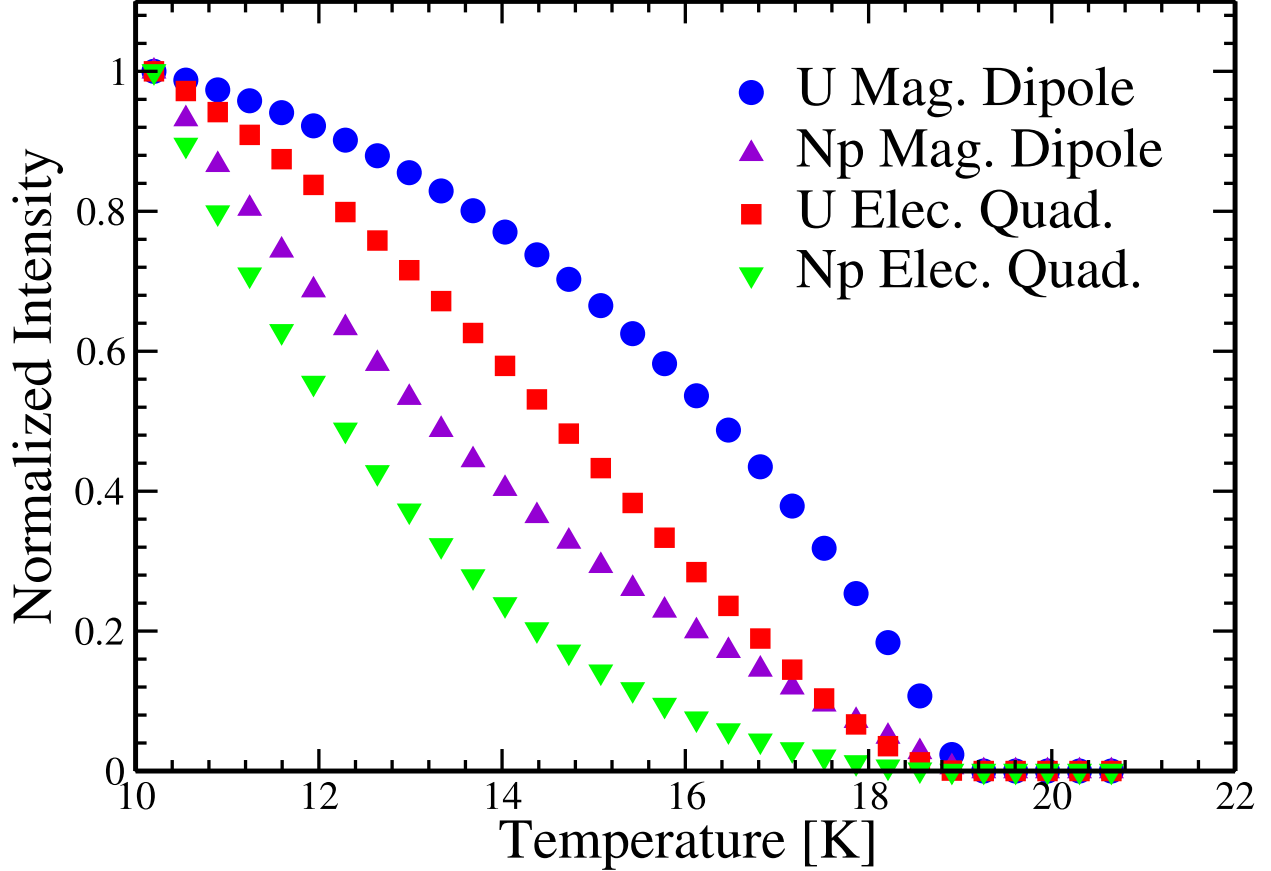


FIG. 9: Calculated temperature dependence of the normalized RXS intensity from U and Np dipoles and quadrupoles for $\text{U}_{0.75}\text{Np}_{0.25}\text{O}_2$.

with U dipoles ordering more quickly than all other moments. This remains true if $K(\text{U-U})$ is varied. Increasing $K(\text{U-U})$ mainly increases the curvature of the red squares in the figure, i.e. it accelerates the ordering of U quadrupoles. However, U dipoles always prevail near T_N , because of their smaller β exponent.

As far as the specific heat C is concerned, a quantitative understanding of the measured curve is difficult for at least two reasons. The first is that the sample dependence of C suggests that slight inhomogeneities in the sample may have pronounced effects on C . Besides being difficult to quantify and characterize, inhomogeneities cannot be included in a VCA calculation, as disorder is averaged out in the VCA. The second reason is that the measured C implies that the magnetic entropy S at T_N is remarkably reduced with respect to what expected ($S = k_B(0.25 \ln(4) + 0.75 \ln(3))$ per actinide ion), while the measured S is lower than $k_B \ln(2)$ per actinide ion (entropy reduction is observed in pure UO_2 and NpO_2 as well,

although the reduction is smaller). Thus, it is *a priori* impossible for any mean-field model such as the VCA to reproduce the measured C quantitatively. A qualitative feature of C whose origin is understandable within the VCA is the presence of slight oscillations below T_N . These seem to reflect the onset of contributions to the free energy from the "delayed" ordering of Np ions. These contribute little to the main peak of C at T_N , and produce features below T_N when their ordering begins to become appreciable.

The VCA provides a qualitatively satisfactory theoretical framework for $\text{U}_{0.75}\text{Np}_{0.25}\text{O}_2$, yet there is one point (besides the entropy reduction problem) which is difficult to understand. This is the low value of the saturation ordered moment of Np ions. There appears to be no way to obtain a moment as low as $0.6\mu_B$ with the observed $3\text{-}\mathbf{k}$ structure.²² This problem would remain even if theoretical approaches different from the VCA were used, as it is associated with the structure of the single-ion CF states of Np. These appear to carry a moment along $\langle 111 \rangle$ always much larger than $0.6\mu_B$, no matter whether the CF is varied or whether quadrupole interactions are included. In particular, since the dipole and quadrupole order parameters appearing in the $3\text{-}\mathbf{k}$ structure commute, the bare CF value of the moment cannot be reduced by quadrupolar interactions. This would not be true if the structure was $1\text{-}\mathbf{k}$.

The experiments on the mixed oxides have shown that at the 25% Np doping ($x = 0.25$) the transverse nature of the $3 - \mathbf{k}$ transition predominates, despite the fact that in pure NpO_2 the ordering of the quadrupoles is longitudinal $3 - \mathbf{k}$. Although the agreement in the top frame of Fig. 6 is not outstanding, it must be remembered that these experiments were performed on an off-specular reflection [the (112) from a (111) face] and this creates more difficulties experimentally than when a specular reflection is examined, as was the case in pure NpO_2 .¹⁷ The crucial aspect is that the maximum and minimum for azimuthal scans agree with the calculations for a transverse $3 - \mathbf{k}$ quadrupolar ordering and completely disagree for the longitudinal model. This change across the solid solutions, from transverse in UO_2 to longitudinal in NpO_2 also gives a possible mechanism for the unusual effects found in the range $0.50 < x < 0.75$ [Refs. 22,23,24] as with increasing Np concentration increasing frustration can be expected between these competing quadrupolar interactions. It will therefore be particularly interesting to try and observe the quadrupolar ordering in the compositions with higher Np content.

Finally, with these observations of the quadrupolar ordering in the mixed oxides we note

in each case the Lorentzian squared shape of the resonances and their displacement to lower energy by about 2 eV (see Figs. 4 and 5). They arise from the $F^{[2]}$ term in the RXS cross section^{25,26} and have also been observed in the work we reported on high-order terms in multi- \mathbf{k} structures.³¹ The strong similarity between these signals and those found¹⁷ in pure NpO_2 suggests that in NpO_2 as well the principle RXS signal arises from a quadrupole signal, and not a more complicated process, as suggested recently.

Acknowledgments

The authors wish to thank Matt Longfield for his help in the early part of these experiments. SBW and PJ would like to thank the European Commission for support in the frame of the ‘Training and Mobility of Researchers’ programme. Part of this work was made possible thanks to the support of the European Community-Access to Research Infrastructures action of the Improving Human Potential Programme (IHP) in allowing access to the Actinide User Laboratory at the Institute for Transuranium-Karlsruhe under the contract HPRICT-200100118.

APPENDIX: AZIMUTHAL DEPENDENCE

In a cubic $3\mathbf{k}$ structure the complete star of $\mathbf{k} = \langle k00 \rangle$ is simultaneously present in each volume element. Therefore there is only one k-domain. However, several orientations of the Fourier components of the magnetic moment relative to the corresponding wave vector are possible. In particular, there are one longitudinal and two transverse directions.

The longitudinal orientation is unique, so for this structure there is only one S-domain. This would be the structure of NpO_2 *if there was a magnetic dipole moment*. In the transverse case, there are two possible orientations which may be converted into each other by applying crystallographic symmetries. This leads to 2 equivalent but distinct S-domains. This is the case in UO_2 .

Below, we calculate the quadrupolar ($F^{[2]}$ term of the cross section) scattering from these 3 constructions.

We assume the crystal structure is FCC with 4 atoms per unit cell. For each atom in turn we can calculate the moment direction at this position for the longitudinal and transverse

Atom	Long.	Trans. Domain A	Trans. Domain B
$(0, 0, 0)$	$\boldsymbol{\mu}_1 = (1, 1, 1)$	$\boldsymbol{\mu}_1 = (1, 1, 1)$	$\boldsymbol{\mu}_1 = (1, 1, 1)$
$(\frac{1}{2}, \frac{1}{2}, 0)$	$\boldsymbol{\mu}_2 = (\bar{1}, \bar{1}, 1)$	$\boldsymbol{\mu}_2 = (1, \bar{1}, \bar{1})$	$\boldsymbol{\mu}_1 = (\bar{1}, 1, \bar{1})$
$(\frac{1}{2}, 0, \frac{1}{2})$	$\boldsymbol{\mu}_3 = (\bar{1}, 1, \bar{1})$	$\boldsymbol{\mu}_3 = (\bar{1}, \bar{1}, 1)$	$\boldsymbol{\mu}_3 = (1, \bar{1}, \bar{1})$
$(0, \frac{1}{2}, \frac{1}{2})$	$\boldsymbol{\mu}_4 = (1, \bar{1}, \bar{1})$	$\boldsymbol{\mu}_4 = (\bar{1}, 1, \bar{1})$	$\boldsymbol{\mu}_4 = (\bar{1}, \bar{1}, 1)$

TABLE I: Moment directions on the four atoms of the unit cell for the single longitudinal and two transverse S-domains

domains (See Figure 1). The resulting directions are given in Table I.

To form the scattering tensor for quadrupole scattering we first evaluate the quadrupole operator \mathbf{Q}_{ij} which in cartesian coordinates is given by

$$\mathbf{Q}_{ij} = \mu_i \mu_j - \frac{1}{3} \delta_{ij} \sum_k (\mu_k \mu_k) \quad (\text{A.1})$$

This matrix is symmetric and traceless. For all of the above structures $\mu_i^2 = 1, \forall i$, which leads to the general form

$$\mathbf{Q} = \begin{pmatrix} 0 & \mu_x \mu_y & \mu_x \mu_z \\ \mu_x \mu_y & 0 & \mu_y \mu_z \\ \mu_x \mu_z & \mu_y \mu_z & 0 \end{pmatrix} \quad (\text{A.2})$$

Evaluating this for the 3 S-domains from the moment directions given in Table I gives scattering tensors for each atom in the unit cell given by Table II for the quadrupole moment.

From these the structure factor can be created as

$$\mathbf{f} = \sum_n \mathbf{T}_n e^{i\mathbf{q} \cdot \mathbf{r}}, \quad (\text{A.3})$$

which for the Bragg reflection $(1, 1, 2)$ gives

$$\mathbf{f}_{(112)} = \mathbf{T}_1 + \mathbf{T}_2 - \mathbf{T}_3 - \mathbf{T}_4 \quad (\text{A.4})$$

yielding scattering tensors of the form

$$\mathbf{f}_{(112)}^L = \begin{pmatrix} 0 & 1 & 0 \\ 1 & 0 & 0 \\ 0 & 0 & 0 \end{pmatrix} \quad (\text{A.5})$$

Atom	Long.	Trans. Domain A	Trans. Domain B
$(0, 0, 0)$	$\begin{pmatrix} 0 & 1 & 1 \\ 1 & 0 & 1 \\ 1 & 1 & 0 \end{pmatrix}$	$\begin{pmatrix} 0 & 1 & 1 \\ 1 & 0 & 1 \\ 1 & 1 & 0 \end{pmatrix}$	$\begin{pmatrix} 0 & 1 & 1 \\ 1 & 0 & 1 \\ 1 & 1 & 0 \end{pmatrix}$
$(\frac{1}{2}, \frac{1}{2}, 0)$	$\begin{pmatrix} 0 & 1 & \bar{1} \\ 1 & 0 & \bar{1} \\ \bar{1} & \bar{1} & 0 \end{pmatrix}$	$\begin{pmatrix} 0 & \bar{1} & \bar{1} \\ \bar{1} & 0 & 1 \\ \bar{1} & 1 & 0 \end{pmatrix}$	$\begin{pmatrix} 0 & \bar{1} & 1 \\ \bar{1} & 0 & \bar{1} \\ 1 & \bar{1} & 0 \end{pmatrix}$
$(\frac{1}{2}, 0, \frac{1}{2})$	$\begin{pmatrix} 0 & \bar{1} & 1 \\ \bar{1} & 0 & \bar{1} \\ 1 & \bar{1} & 0 \end{pmatrix}$	$\begin{pmatrix} 0 & 1 & \bar{1} \\ 1 & 0 & \bar{1} \\ \bar{1} & \bar{1} & 0 \end{pmatrix}$	$\begin{pmatrix} 0 & \bar{1} & \bar{1} \\ \bar{1} & 0 & 1 \\ \bar{1} & 1 & 0 \end{pmatrix}$
$(0, \frac{1}{2}, \frac{1}{2})$	$\begin{pmatrix} 0 & \bar{1} & \bar{1} \\ \bar{1} & 0 & 1 \\ \bar{1} & 1 & 0 \end{pmatrix}$	$\begin{pmatrix} 0 & \bar{1} & 1 \\ \bar{1} & 0 & \bar{1} \\ 1 & \bar{1} & 0 \end{pmatrix}$	$\begin{pmatrix} 0 & 1 & \bar{1} \\ 1 & 0 & \bar{1} \\ \bar{1} & \bar{1} & 0 \end{pmatrix}$

TABLE II: Scattering tensors for the four atoms in the FCC unit cell for the longitudinal and transverse cases.

$$\mathbf{f}_{(112)}^A = \begin{pmatrix} 0 & 0 & 0 \\ 0 & 0 & 1 \\ 0 & 1 & 0 \end{pmatrix}$$

$$\mathbf{f}_{(112)}^B = \begin{pmatrix} 0 & 0 & 1 \\ 0 & 0 & 0 \\ 1 & 0 & 0 \end{pmatrix}$$

This can be evaluated to give a total structure factor of

$$\mathbf{F}_{(112)}^{[2]} = \boldsymbol{\epsilon}' \cdot \mathbf{f}_{(112)} \cdot \boldsymbol{\epsilon}, \quad (\text{A.6})$$

where $\boldsymbol{\epsilon}$ and $\boldsymbol{\epsilon}'$ are the polarization vectors of the incident and scattered beams, respectively. Here we consider only $\sigma \rightarrow \sigma$ scattering, as the $\sigma \rightarrow \pi$ channel is dominated by magnetic

scattering ($F^{[1]}$) term.

To evaluate this, first we construct a coordinate system of the crystal. We therefore, construct 3 unit vectors based on the reciprocal space vectors \mathbf{q} (the scattering vector) and $\mathbf{k}_{\text{azref}}$ (the azimuth reference vector), $\hat{\mathbf{c}}_1$, $\hat{\mathbf{c}}_2$ and $\hat{\mathbf{c}}_3$. These are related by,

$$\begin{aligned}\hat{\mathbf{c}}_3 &= -\frac{\mathbf{q}}{|\mathbf{q}|} \\ \hat{\mathbf{c}}_2 &= \hat{\mathbf{c}}_3 \times \left(\frac{\mathbf{k}_{\text{azref}}}{|\mathbf{k}_{\text{azref}}|} \right) \\ \hat{\mathbf{c}}_1 &= \hat{\mathbf{c}}_2 \times \hat{\mathbf{c}}_3.\end{aligned}\tag{A.7}$$

We then do a rotation around $\hat{\mathbf{c}}_3$ to transform into the coordinate system of Blume and Gibbs.²⁹ We therefore obtain 3 new unit vectors of the form,

$$\begin{aligned}\hat{\mathbf{u}}_3 &= \hat{\mathbf{c}}_3 \\ \hat{\mathbf{u}}_2 &= \hat{\mathbf{c}}_1 \sin \phi + \hat{\mathbf{c}}_2 \cos \phi \\ \hat{\mathbf{u}}_1 &= \hat{\mathbf{c}}_1 \cos \phi - \hat{\mathbf{c}}_2 \sin \phi.\end{aligned}\tag{A.8}$$

which again are linear combinations of the reciprocal space vectors \mathbf{q} , $\mathbf{k}_{\text{azref}}$ and the cross product of these two. We can then define the polarization vectors for the incident and exit beams in the new coordinate system. For σ polarization this is simply equal to the unit vector $\hat{\mathbf{u}}_2$, i.e. the polarization vector is normal to the scattering plane (given by the cross product of the scattering vector and the azimuthal reference vector). For π polarization the Bragg angle of the reflection has to be taken into consideration. This is included here for completeness but is not used for these calculations. We therefore have the polarization vectors in the rotated coordinate system given by

$$\hat{\mathbf{e}}_\sigma = \hat{\mathbf{e}}'_\sigma = \hat{\mathbf{u}}_2\tag{A.9}$$

$$\hat{\mathbf{e}}_\pi = \hat{\mathbf{u}}_1 \sin \theta_B - \hat{\mathbf{u}}_3 \cos \theta_B\tag{A.10}$$

$$\hat{\mathbf{e}}'_\pi = -\hat{\mathbf{u}}_1 \sin \theta_B - \hat{\mathbf{u}}_3 \cos \theta_B\tag{A.11}$$

Given these vectors equation A.6 can be evaluated to give the amplitude of the scattering for each required ϕ value.

¹ W.M. Jones, J. Gordon, and E.A. Long, *J. Chem. Phys.* **20**, 695 (1952).

- ² A. Arrot and J.E. Goldman, *Phys. Rev.* **108**, 948 (1957).
- ³ B.T.M. Willis and R.I. Taylor, *Phys. Lett.* **17**, 188 (1965).
- ⁴ B.C. Frazer, G. Shirane, D.E. Cox, and C.E. Olsen, *Phys. Rev.* **140**, A1448 (1965).
- ⁵ R.A. Cowley and G. Dolling, *Phys. Rev.* **167**, 464 (1968).
- ⁶ S.J. Allen, *Phys. Rev.* **167**, 492 (1968).
- ⁷ J. Faber and G.H. Lander, *Phys. Rev. B* **14**, 1151 (1976).
- ⁸ P. Bulet, J. Rossat-Mignod, S. Quezel, O. Vogt, J.C. Spirlet, and J. Rebizant, *J. Less-Common Met.* **121**, 121 (1986).
- ⁹ G. Amoretti, A. Blaise, R. Caciuffo, J.M. Fournier, M.T. Hutchings, R. Osborn, and A.D. Taylor, *Phys. Rev. B* **40**, 1856 (1989).
- ¹⁰ R. Caciuffo, G. Amoretti, P. Santini, G.H. Lander, J. Kulda, and P. de V. Du Plessis, *Phys. Rev. B* **59**, 13892 (1999).
- ¹¹ D.W. Osborne and E.F. Westrum, *J. Chem. Phys.* **21**, 1884 (1953).
- ¹² J.W. Ross and D.J. Lam *J. Appl. Phys.* **38**, 1451 (1967).
- ¹³ B.D. Dunlap, G.M. Kalvius, D.J. Lam, and M.B. Brodsky, *J. Phys. Chem. Solids* **29**, 1365 (1968).
- ¹⁴ D.E. Cox and B.C. Frazer, *J. Phys. Chem. Solids* **28**, 1649 (1967).
- ¹⁵ L. Heaton, M.H. Müller, and J.M. Williams, *J. Phys. Chem. Solids* **28**, 1651 (1967).
- ¹⁶ A. Boeuf, R. Caciuffo, J.M. Fournier, L. Manes, J. Rebizant, F. Rustichelli, J.C. Spirlet, and A. Wright, *Phys. Stat. Solidi* **79**, K1 (1983).
- ¹⁷ J. A. Paixão, C. Detlefs, M.J. Longfield, R. Caciuffo, P. Santini, N. Bernhoeft, J. Rebizant, and G.H. Lander, *Phys. Rev. Lett.* **89**, 187202 (2002); R. Caciuffo, J. A. Paixão, C. Detlefs, M.J. Longfield, P. Santini, N. Bernhoeft, J. Rebizant, and G.H. Lander, *J. of Phys.: Cond. Matter* **15**, S2287 (2003).
- ¹⁸ R. Caciuffo, G.H. Lander, J.C. Spirlet, J.M. Fournier, and W.F. Kuhs, *Solid State Comm.* **64**, 149 (1987).
- ¹⁹ D. Mannix, G.H. Lander, J. Rebizant, R. Caciuffo, N. Bernhoeft, E. Lidström, and C. Vettier, *Phys. Rev. B* **60**, 15187 (1999).
- ²⁰ P. Santini and G. Amoretti, *Phys. Rev. Lett.* **85**, 2188 (2000).
- ²¹ A. Kiss and P. Fazekas *Phys. Rev. B* **68**, 174425 (2003).
- ²² A. Boeuf, R. Caciuffo, M. Pagès, J. Rebizant, F. Rustichelli, and A. Tabuteau, *Europhys. Lett.*

- 3**, 221 (1987).
- ²³ A. Tabuteau, M. Pagès, A. Boeuf, J. Rebizant, L. Manes, R. Caciuffo, and F. Rustichelli, *J. de Phys. Lett.*, **45** 373 (1984).
- ²⁴ A. Tabuteau, J. Jové, M. Pagès, C.H. de Novion and J. Gal, *Solid St. Comm.*, **50**, 357 (1984).
- ²⁵ J.P. Hannon, G.T. Trammell, M. Blume, and D. Gibbs, *Phys. Rev. Lett.* **61**, 1245 (1988); *ibid* **62**, 2644 (E) (1989).
- ²⁶ J.P. Hill and D.F. McMorrow, *Acta Cryst. A* **52**, 236 (1996).
- ²⁷ M. Blume, *Resonant Anomalous X-ray Scattering* Edited by G. Materik, C. J. Sparks and K. Fisher Elsevier Science, 495 (1994)
- ²⁸ M. Blume, *J. Appl. Phys.* **57**, 3615 (1985).
- ²⁹ M. Blume and D. Gibbs, *Phys. Rev. B* **37**, 1779 (1988).
- ³⁰ D.H. Templeton and L.K. Templeton, *Acta Crystallogr. Sect. A* **41**, 133 (1985).
- ³¹ M. J. Longfield, J. A. Paixão, N. Bernhoeft, and G. H. Lander, *Phys. Rev. B* **66**, 054417 (2002).
- ³² G. Amoretti, A. Blaise, R. Caciuffo, D. Di Cola, J.M. Fournier, M.T. Hutchings, G.H. Lander, R. Osborn, A. Severing, and A.D. Taylor, *J. Phys. Condens. Matter* **4**, 3459 (1992).
- ³³ G. Solt and P. Erdös, *J. Magn. Magn. Mater.* **15-18**, 57 (1980).
- ³⁴ R. Caciuffo, G. Amoretti, J.M. Fournier, A. Blaise, R. Osborn, A.D. Taylor, J. Larroque, and M.T. Hutchings, *Solid State Comm.* **69**, 197 (1991).
- ³⁵ P. Santini and G. Amoretti, *J. Phys. Soc. Jpn.* **71** Suppl., 11 (2002).
- ³⁶ P. Giannozzi and P. Erdös, *J. Magn. Magn. Mater.* **67**, 75 (1987).
- ³⁷ J. Jensen, and A.R. Mackintosh, *Rare Earth Magnetism*, Clarendon Press, Oxford (1991).
- ³⁸ S.W. Lovesey, E. Balcar, C. Detlefs, G. van der Laan, D.S. Sivia, U. Staub, *J. Phys. Cond. Mat.* **15**, 4511 (2003)

